

Supplementary Information Text

This supplementary information contains details of the OpenSim model and validation. In Supplementary Information A, we first discuss updates to the original musculoskeletal model developed by Mortensen et. al. (14). We then discuss our ligament model and the ligament properties, which were taken from previous experimental and modeling papers in Supplementary Information B. We then discuss validation of the ligaments in intersegmental simulations of the OpenSim model (Supplementary Information C) and the evaluation of the full OpenSim model against experimental mild impacts (Supplemental Information D).

Supplementary Information A: OpenSim Musculoskeletal Model

Model Musculature. The first OpenSim head and neck model was developed by Vasavada and subsequently improved by Mortensen to explore moment contributions of the neck muscles (13, 14). The Mortensen extended the original model by including the multifidus and hyoid muscles. The hyoid muscles, which all have attachments to the hyoid bone were instead attached directly to the vertebrae or skull. The hyoid bone has a complicated kinematic relationship with the cervical spine and the skull that is not easily modeled. Furthermore, we included a wrapping surface for the sternocleidomastoid subvolumes that represented the intersection of the sternocleidomastoid with the intermediate tendon of the omohyoid. As in the Mortensen model, we only modeled the superior belly of the omohyoid. The baseline model is available through SimTK: https://simtk.org/projects/kuo_head_neck

Model Vertebrae. The seven vertebrae (C7 through C1) of the cervical spine, the skull (C0), and the torso (thoracic vertebra T1 and below) were all represented by rigid body elements. The inertial properties of the cervical vertebrae were taken from (30) and include the inertial properties of the vertebrae and surrounding tissue. The skull inertial properties were taken from Yoganandan 2009 (40), which matched our previous work with this data (4). Inertial properties are presented in Table A1.

Model Kinematics. In the original model, adjacent cervical vertebrae were joined using a three degree-of-freedom rotational joint. However, intervertebral rotations were constrained to three independent generalized coordinates resulting in smooth cervical spine curvatures throughout the range of motion. For our study, we note that previous investigations have observed different cervical spine curvature (26, 27, 29) or buckling (41–43) patterns during whiplash impacts and axial loads respectively, and thus we believed imposing cervical spine constraints would not be valid. Thus, as is stated in the manuscript, we removed kinematic constraints between cervical vertebrae C2-C7 and at the C7-T1 intervertebral joint and we represented upper cervical vertebral joint C2-C1 and C1-C0 with single degree-of-freedom rotational joints in primary axes of rotation (axial left/right rotations and sagittal flexion/extension rotations respectively). This yielded a total of 20 independent degrees-of-freedom. Cervical spine intervertebral joint degrees-of-freedom are shown in Figure S1 in Supplementary Information B.

Table S1: Cervical Spine Inertial Properties

Rigid Body	Mass	Moment of Inertia Anterior-Posterior (I_{xx})	Moment of Inertia Left-Right (I_{yy})	Moment of Inertia Superior-Inferior (I_{zz})
Torso*	60.0 kg	16,130 kg-cm ²	16,130 kg-cm ²	3,000 kg-cm ²
^[27] Cervical Vertebra C7	0.400 kg	21.0 kg-cm ²	6.0 kg-cm ²	26.0 kg-cm ²
^[27] Cervical Vertebra C6	0.226 kg	2.0 kg-cm ²	5.3 kg-cm ²	9.7 kg-cm ²
^[27] Cervical Vertebra C5	0.269 kg	6.0 kg-cm ²	4.8 kg-cm ²	14.0 kg-cm ²
^[27] Cervical Vertebra C4	0.205 kg	1.5 kg-cm ²	3.7 kg-cm ²	5.7 kg-cm ²
^[27] Cervical Vertebra C3	0.156 kg	3.3 kg-cm ²	2.6 kg-cm ²	4.3 kg-cm ²
^[27] Cervical Vertebra C2	0.156 kg	3.3 kg-cm ²	2.6 kg-cm ²	4.3 kg-cm ²
^[27] Cervical Vertebra C1	0.156 kg	3.3 kg-cm ²	2.6 kg-cm ²	4.3 kg-cm ²
^[28] Skull	4.30 kg	207.3 kg-cm ²	226.1 kg-cm ²	150.0 kg-cm ²

* Because the torso was fixed in our simulations, the inertial properties of the torso did not affect the simulation results. These should be properly adjusted for future use.

Supplementary Information B: Ligament Modeling and Parameters

Ligament Model. The ligament model represented by equations 1-4 in the main manuscript is based on previous literature (21, 34–36). There have been several constitutive models developed to represent the non-linear force-length relationship of the ligaments; however, all of them fundamentally capture the general characteristics of the toe and linear regions, which we represent with a piece-wise linear function. While we did not model the yield region, ligament failure can be determined from simulations by identifying when yield strain or stress is achieved. However, as a caveat, previous literature has reported that failure values also have a lengthening-rate dependence (typically larger yield stresses and lower yield strains) (17, 19, 44).

Included Ligaments. Ligaments in the lower cervical spine (cervical vertebrae C2 through C7) are similar to those found in the thoracic spine. At each intervertebral joint, we have modeled six ligaments comprised of eight linear elements (two ligaments are represented by a pair of linear elements). These ligaments are the anterior longitudinal ligament (ALL), posterior longitudinal ligament (PLL), ligamentum flavum (LF, paired), capsular ligaments (CL, paired), interspinous ligament (ISL), and ligamentum nuchae (LN). These are shown in Figure S2. These ligaments are represented as single linear elements through the center of the ligament body (or in the case of the capsular ligament, through the center of capsule). This is similar to how muscles are modeled in the OpenSim model.

The ALL, PLL, and LN are continuous ligaments running along the length the spine. However, the geometry of these ligaments change at each spinal level, and some ligament fibers travel only between adjacent vertebrae. As such, we have chosen to represent these ligaments as individual linear elements between adjacent vertebrae. The ligamentum nuchae is unique to the cervical spine, though it is a continuation of the supraspinous ligament in the thoracic spine. Finally, the intertransverse ligament connecting the transverse processes of adjacent vertebrae are relatively small in the cervical spine, and are thus not modeled.

In addition to ligaments in the lower cervical spine, we included a pair of linear elements representing fibers of the annulus fibrosus (AF), which are part of the intervertebral discs. The AF in the cervical spine anatomically distinct from the AF in the thoracic spine. In the cervical spine, the AF is concentrated on the anterior side of the vertebrae. Furthermore, the AF fibers are well integrated with the ALL (45, 46). The orientation of the AF fibers runs at 60°-65° from the horizontal plane, and it has been suggested that these fibers provide resistance to axial rotations in addition to providing support for the disc nucleus (45, 47). We modeled our AF fibers only on the anterior side with each pair running 60° from the horizontal in opposite directions and crossing at the mid-sagittal plane.

The upper cervical spine (between C2 and the skull) are anatomically distinct from the rest of the spine. The structure of the C2 and C1 vertebrae allow for large ranges of motion in axial rotation (C2-C1 atlanto-axial joint) and flexion/extension (C1-C0 atlanto-occipital joint). Due to the large relative motion of the adjacent vertebrae, there are no intervertebral discs at these levels. Furthermore, the ligaments form a much more complex structure. In our model, we have included the anterior and posterior atlanto-atlas membranes (AAA and PAA respectively), the anterior and posterior atlanto-occipital membranes (AAO and PAO respectively), capsular ligaments (CL), alar ligaments (AL), apical ligament (API), tectorial membrane (TM), and cruciate ligament (CLT).

The anterior membranes (AAA and AAO) are continuations of the ALL, while the posterior membranes (PAA and PAO) are continuations of the LF. The remaining ligaments have

attachments on the dens, a protrusion of the C2 vertebrae that allows for C1 axial rotation. There are many other minor ligaments within the upper cervical spine (accessory ligaments, barking ligament); however, we have not included them because they are relatively weak or small compared to the ligaments described here.

Fitting Parameters. To fit parameters associated with the constitutive model defined by equations 1-4, we briefly reviewed literature on cervical spine ligament material properties (17, 18, 47–52, 19, 21, 34–36, 44–46). Unfortunately, different researchers report different values in the constitutive model. For example: Bass et. al. (52) and Shim et. al. (18) only report yield stresses and strains; Yoganandan et. al. (34) report only linear region modulus; Chazal et. al. (53) report linear region modulus and failure stresses and strains; and Mattucci et. al. (44, 48) report toe strain and toe region modulus in addition to linear region and failure values. Furthermore, several researchers report un-normalized results in terms of forces and displacements (17–19, 21).

To compile previous literature, we primarily extracted linear region modulus, toe region modulus, and toe region strain. For studies that only report failure values (stress and strain or force and displacement), we estimated modulus or stiffness as the ratio of failure stress to failure strain, or the ratio of failure force to failure displacement. We also compiled geometrical values for the ligaments, namely cross-sectional areas and rest lengths (34–36, 49). These were used to properly non-dimensionalize studies that reported material properties in terms of force and displacement.

With material properties uniformly converted to our piecewise linear model and non-dimensionalized stress and strain values, we then fit our model to compiled data. First, we had to determine the lengthening rate dependence, as studies performed material characterization at different rates. We used reported lengthening rates (v^{lig}) and associated linear range moduli (E_{lin}) to determine m_{rate} . One assumption in our model is that the toe range moduli (E_{toe}) scales with the linear range moduli (E_{lin}) and toe strain does not depend on lengthening rate (ϵ_{toe}). While this might not be true (given that the failure strain and stress have lengthening rate dependencies), there is insufficient data from previous literature to fit these values. Furthermore, we used 10mm/s as the representative quasi-static lengthening rate as this was the minimum lengthening rate tested for several ligaments (21).

With the fit lengthening-rate dependence m_{rate} , we could scale high-rate experimental parameters to fit static parameters. This procedure is visualized for the Anterior Longitudinal Ligament (ALL) segment in the intervertebral joint C7-C6 as an example in Figure S3. Fit parameters for each ligament at each intervertebral level are given in Tables S2 and S3.

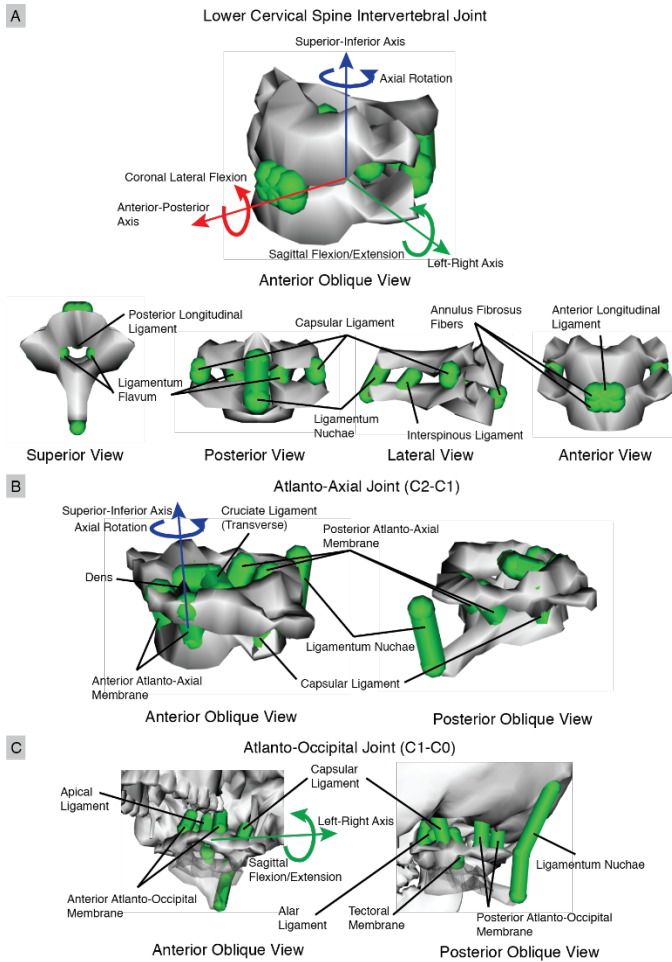


Figure S2: Cervical Spine Ligaments and Kinematics: (A) Lower cervical spine is represented by intervertebral joints T1-C7 through C3-C2. These joints are modeled with three rotational degrees of freedom about the anatomical axes and taken from Mortensen 2018 (13). There are six ligaments represented by eight linear elements, as well as the annulus fibrosus of the disc represented by two linear elements at 60° from the horizontal. The upper cervical spine, represented by the (B) atlanto-axial (C2-C1) joint and the (C) atlanto-occipital (C1-C0) joint are anatomically unique compared to the lower cervical spine. Of particular note, there are no intervertebral discs at this spinal level. The C2-C1 has significant compliance in axial rotation about the superior-inferior axis, with vertebrae C1 rotating about the dens of the C2 vertebra. The C1-C0 has significant compliance in sagittal flexion/extension about the left-right axis, with the skull's occipital condyles articulating on the superior facets of the C1 vertebra.

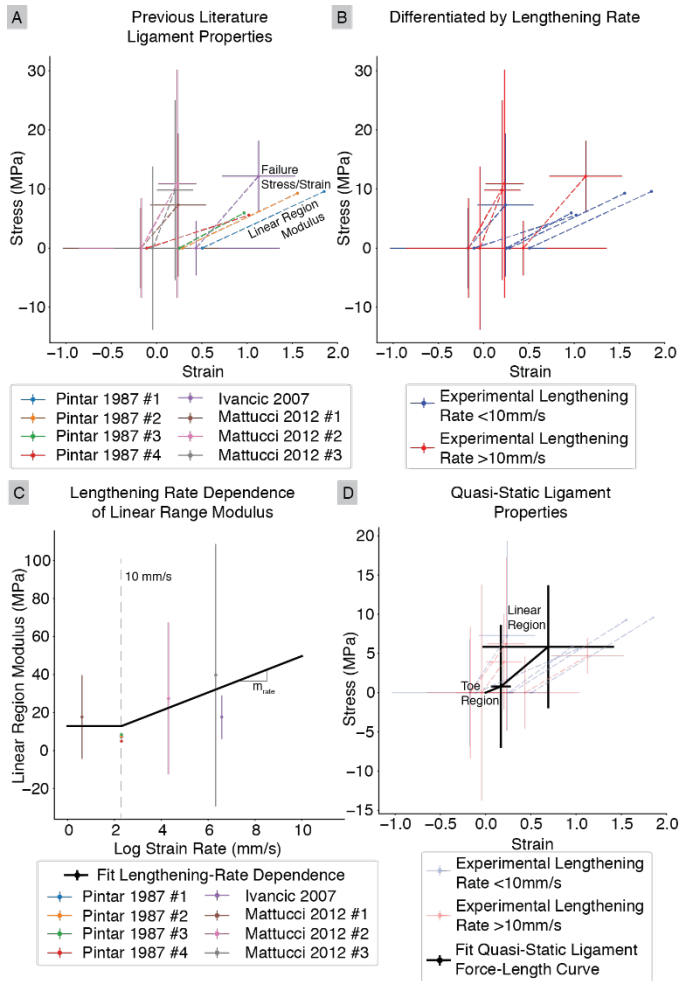


Figure S3: Fitting Ligament Material Properties: (A) Ligament material properties from previous literature were extracted. We primarily computed the linear region modulus (MPa), which in many reports were found by taking the ratio between the failure stress and failure strain. (B) Cervical spine ligaments are known to have a strong lengthening-rate relationship, and many studies report ligament material properties at high rates. For our study, we considered lengthening rates below 10mm/s as quasi-static, as this was the minimum lengthening rate for several ligaments previously studied. When we differentiate the previously reported stress-strain curves by lengthening rate, we observe that studies using the highest lengthening rates had larger linear region moduli. (C) Fitting a linear relationship for the linear region modulus against the log of the lengthening rate, we can solve for m_{rate} from equation 7. (D) Finally, we scaled high lengthening-rate properties and fit quasi-static material properties for the ligaments.

Table S2: Cervical Spine Ligament Material Properties (T1-C4)

Intervertebral Joint T1-C7

Ligament	Rest Length (l_0)	Cross-Sectional Area ($A^{(0)}$)	Toe Strain (ϵ_{toe})	Toe Modulus (E_{toe})	Linear Modulus (E_{lin})	Lengthening Rate Scaling (m_{rate})
Anterior Longitudinal Ligament	4.085 mm	12.3 mm ²	27%	4.26 MPa	8.52 MPa	1.33
Posterior Longitudinal Ligament	4.085 mm	15.6 mm ²	17%	5.02 MPa	10.04 MPa	1.26
Ligamentum Flavum	9.420 mm	21.3 mm ²	26%	3.65 MPa	7.85 MPa	1.17
Capsular Ligament	4.329 mm	55.5 mm ²	17%	0.99 MPa	1.98 MPa	1.17
Interspinous Ligament	9.795 mm	23.9 mm ²	13%	1.26 MPa	2.53 MPa	1.29
Ligamentum Nuchae	21.586 mm	10.0 mm ²	5%	25 MPa	50 MPa	1.20
Annulus Fibrosus Fibers	8.983 mm	100.0 mm ²	5%	25 MPa	50 MPa	1.50

Intervertebral Joint C7-C6

Ligament	Rest Length (l_0)	Cross-Sectional Area ($A^{(0)}$)	Toe Strain (ϵ_{toe})	Toe Modulus (E_{toe})	Linear Modulus (E_{lin})	Lengthening Rate Scaling (m_{rate})
Anterior Longitudinal Ligament	4.056 mm	11.75 mm ²	27%	4.23 MPa	8.45 MPa	1.38
Posterior Longitudinal Ligament	4.056 mm	14.65 mm ²	17%	4.84 MPa	9.68 MPa	1.37
Ligamentum Flavum	9.145 mm	20.70 mm ²	26%	3.44 MPa	6.88 MPa	1.22
Capsular Ligament	4.087 mm	52.39 mm ²	17%	1.04 MPa	2.08 MPa	1.15
Interspinous Ligament	11.081 mm	14.54 mm ²	13%	1.73 MPa	3.46 MPa	1.28
Ligamentum Nuchae	13.762 mm	10.0 mm ²	5%	10 MPa	20 MPa	1.20
Annulus Fibrosus Fibers	8.970 mm	100.0 mm ²	5%	25 MPa	50 MPa	1.50

Intervertebral Joint C6-C5

Ligament	Rest Length (l_0)	Cross-Sectional Area ($A^{(0)}$)	Toe Strain (ϵ_{toe})	Toe Modulus (E_{toe})	Linear Modulus (E_{lin})	Lengthening Rate Scaling (m_{rate})
Anterior Longitudinal Ligament	4.074 mm	10.76 mm ²	27%	4.70 MPa	9.40 MPa	1.25
Posterior Longitudinal Ligament	3.857 mm	13.07 mm ²	17%	6.85 MPa	13.71 MPa	1.23
Ligamentum Flavum	7.827 mm	17.83 mm ²	26%	1.99 MPa	3.98 MPa	1.36
Capsular Ligament	3.839 mm	47.19 mm ²	17%	0.77 MPa	1.53 MPa	1.23
Interspinous Ligament	8.714 mm	20.65 mm ²	13%	1.26 MPa	2.52 MPa	1.28
Ligamentum Nuchae	15.687 mm	10.0 mm ²	5%	10 MPa	20 MPa	1.20
Annulus Fibrosus Fibers	8.978 mm	40.0 mm ²	5%	25 MPa	50 MPa	1.50

Intervertebral Joint C5-C4

Ligament	Rest Length (l_0)	Cross-Sectional Area ($A^{(0)}$)	Toe Strain (ϵ_{toe})	Toe Modulus (E_{toe})	Linear Modulus (E_{lin})	Lengthening Rate Scaling (m_{rate})
Anterior Longitudinal Ligament	4.268 mm	10.29 mm ²	27%	4.22 MPa	8.45 MPa	1.43
Posterior Longitudinal Ligament	3.679 mm	11.33 mm ²	17%	7.00 MPa	14.00 MPa	1.35
Ligamentum Flavum	7.604 mm	17.33 mm ²	26%	1.85 MPa	3.69 MPa	1.40
Capsular Ligament	4.662 mm	57.30 mm ²	17%	0.80 MPa	1.59 MPa	1.22
Interspinous Ligament	10.351 mm	11.22 mm ²	13%	2.90 MPa	5.80 MPa	1.12
Ligamentum Nuchae	12.572 mm	10.0 mm ²	5%	10 MPa	20 MPa	1.20
Annulus Fibrosus Fibers	9.067 mm	40.0 mm ²	5%	25 MPa	50 MPa	1.50

* Ligamentum Nuchae and Annulus Fibrosus Fiber properties were estimated from other modeling studies rather than experimental studies or matched to the Interspinous Ligament or Anterior Longitudinal Ligament respectively.

Table S3: Cervical Spine Ligament Material Properties (C4-Skull)

Intervertebral Joint C4-C3

Ligament	Rest Length (l_0)	Cross-Sectional Area ($A^{(0)}$)	Toe Strain (ϵ_{toe})	Toe Modulus (E_{toe})	Linear Modulus (E_{lin})	Lengthening Rate Scaling (m_{lin})
Anterior Longitudinal Ligament	3.612 mm	10.40 mm ²	27%	3.98 MPa	7.96 MPa	1.37
Posterior Longitudinal Ligament	4.159 mm	10.56 mm ²	17%	6.42 MPa	12.83 MPa	1.30
Ligamentum Flavum	8.106 mm	21.35 mm ²	26%	3.20 MPa	6.40 MPa	1.15
Capsular Ligament	4.111 mm	45.77 mm ²	17%	1.32 MPa	2.64 MPa	1.16
Interspinous Ligament	7.829 mm	19.30 mm ²	13%	1.71 MPa	3.42 MPa	1.32
Ligamentum Nuchae	13.509 mm	10.0 mm ²	5%	25 MPa	50 MPa	1.20
Annulus Fibrosus Fibers	8.778 mm	30.0 mm ²	5%	25 MPa	50 MPa	1.50

Intervertebral Joint C3-C2

Ligament	Rest Length (l_0)	Cross-Sectional Area ($A^{(0)}$)	Toe Strain (ϵ_{toe})	Toe Modulus (E_{toe})	Linear Modulus (E_{lin})	Lengthening Rate Scaling (m_{lin})
Anterior Longitudinal Ligament	4.106 mm	11.28 mm ²	27%	4.61 MPa	9.22 MPa	1.35
Posterior Longitudinal Ligament	3.942 mm	9.72 mm ²	17%	8.78 MPa	16.56 MPa	1.22
Ligamentum Flavum	7.599 mm	20.01 mm ²	26%	2.18 MPa	4.35 MPa	1.30
Capsular Ligament	4.116 mm	45.82 mm ²	17%	1.21 MPa	2.42 MPa	1.19
Interspinous Ligament	9.797 mm	9.77 mm ²	13%	2.79 MPa	5.47 MPa	1.19
Ligamentum Nuchae	14.090 mm	10.0 mm ²	5%	10 MPa	20 MPa	1.20
Annulus Fibrosus Fibers	8.992 mm	20.0 mm ²	5%	25 MPa	50 MPa	1.50

Intervertebral Joint C2-C1 (Atlanto-Axial)

Ligament	Rest Length (l_0)	Cross-Sectional Area ($A^{(0)}$)	Toe Strain (ϵ_{toe})	Toe Modulus (E_{toe})	Linear Modulus (E_{lin})	Lengthening Rate Scaling (m_{lin})
Anterior Atlanto-Axial Membrane	11.812 mm	23.84 mm ²	7.6%	5.21 MPa	10.41 MPa	1.30
Posterior Atlanto-Axial Membrane	15.147 mm	10.38 mm ²	8.6%	10.83 MPa	21.65 MPa	1.30
Capsular Ligament	14.936 mm	39.83 mm ²	7.8%	5.87 MPa	10.74 MPa	1.73
Ligamentum Nuchae	22.963 mm	10.0 mm ²	5%	10 MPa	20 MPa	1.20
Cruciate Ligament (Transverse)	20.309 mm	18.57 mm ²	11%	26.92 MPa	53.83 MPa	1.31

Intervertebral Joint C1-C0 (Atlanto-Occipital)

Ligament	Rest Length (l_0)	Cross-Sectional Area ($A^{(0)}$)	Toe Strain (ϵ_{toe})	Toe Modulus (E_{toe})	Linear Modulus (E_{lin})	Lengthening Rate Scaling (m_{lin})
Anterior Atlanto-Occipital Membrane	12.735 mm	44.30 mm ²	12%	0.64 MPa	1.28 MPa	2.56
Posterior Atlanto-Occipital Membrane	13.600 mm	47.72 mm ²	8.4%	0.39 MPa	0.78 MPa	2.85
Capsular Ligament	19.088 mm	38.17 mm ²	7.1%	23.64 MPa	47.28 MPa	1.38
Ligamentum Nuchae	40.050 mm	10.0 mm ²	5%	10 MPa	20 MPa	1.20
Alar Ligament**	10.146 mm	20.96 mm ²	5%	8.05 MPa	16.10 MPa	1.13
Apical Ligament**	13.925 mm	19.03 mm ²	7.8%	10.97 MPa	20.94 MPa	1.75
Tectorial Membrane**	18.520 mm	32.32 mm ²	7.8%	20.99 MPa	40.97 MPa	1.75

* Ligamentum Nuchae and Annulus Fibrosus Fiber properties were estimated from other modeling studies rather than experimental studies or matched to the Interspinous Ligament or Anterior Longitudinal Ligament respectively.

** These ligaments cross from C2 to the skull via the Dens

Supplementary Information C: Cervical Spine Ligament Validation

To validate the cervical spine ligaments, we chose to compare intervertebral segment moment-deflection behavior against previously published experiments (31, 54–56). In these experiments, researchers applied pure moments to functional intervertebral segments (54–56) or whole cervical spine specimens (31) and measured the resulting rotational deflection. For all experiments, muscles were typically excised, leaving the vertebrae, ligaments, and discs. Soft tissue (ligaments and discs) are thus responsible for moment-deflection characteristics. We felt these experiments were ideal for validation because moments depend on both the material and geometrical properties of the soft tissue.

To validate our model, we created matching functional intervertebral models with only vertebrae and associated ligaments. For the upper cervical spine, we created one model with cervical vertebrae C2 through the skull to match Goel et. al. (54). Note, because we chose to model the two joints between cervical vertebrae C2 through the skull with single orthogonal degrees of freedom, their motions could be considered independent. According to Nightingale et. al. (55), the ligamentum nuchae was also excised as this ligament is an insertion point for many posterior muscles. Thus, we also removed the ligamentum nuchae from our functional intervertebral models.

With the models, we prescribed rotations similar to those in previous literature. Lower cervical spine intervertebral segments were rotated from -10° to 10° in coronal lateral flexion about the anterior-posterior axis, sagittal flexion/extension about the left-right axis, and axial rotation about the superior-inferior axis. The upper cervical spine model representing C2 through skull was rotated from -20° to 20° in sagittal flexion/extension about the left-right axis and axial rotation about the superior-inferior axis. Note, coronal lateral flexion rotations about the anterior-posterior axis were not exercised because the C2 through skull model does not have a degree of freedom allowing for that rotational direction. Furthermore, a greater range was exercised in previous literature and in our validations due to the increased compliance in the upper cervical spine (31, 54).

Moments provided by the soft tissue during these rotations were computed using the same method reported in the main manuscript (equation 10). Briefly, this method computes a moment arm for linear force elements using the ratio between the change in rotation angle and the change in length of the linear element (39). The moment is then the moment arm scaled by the force produced. Figures S3 and S4 show the simulated moment-deflection curves for functional intervertebral units overlaid on previous experimental data. Furthermore, moment contributions from individual ligament linear elements are included.

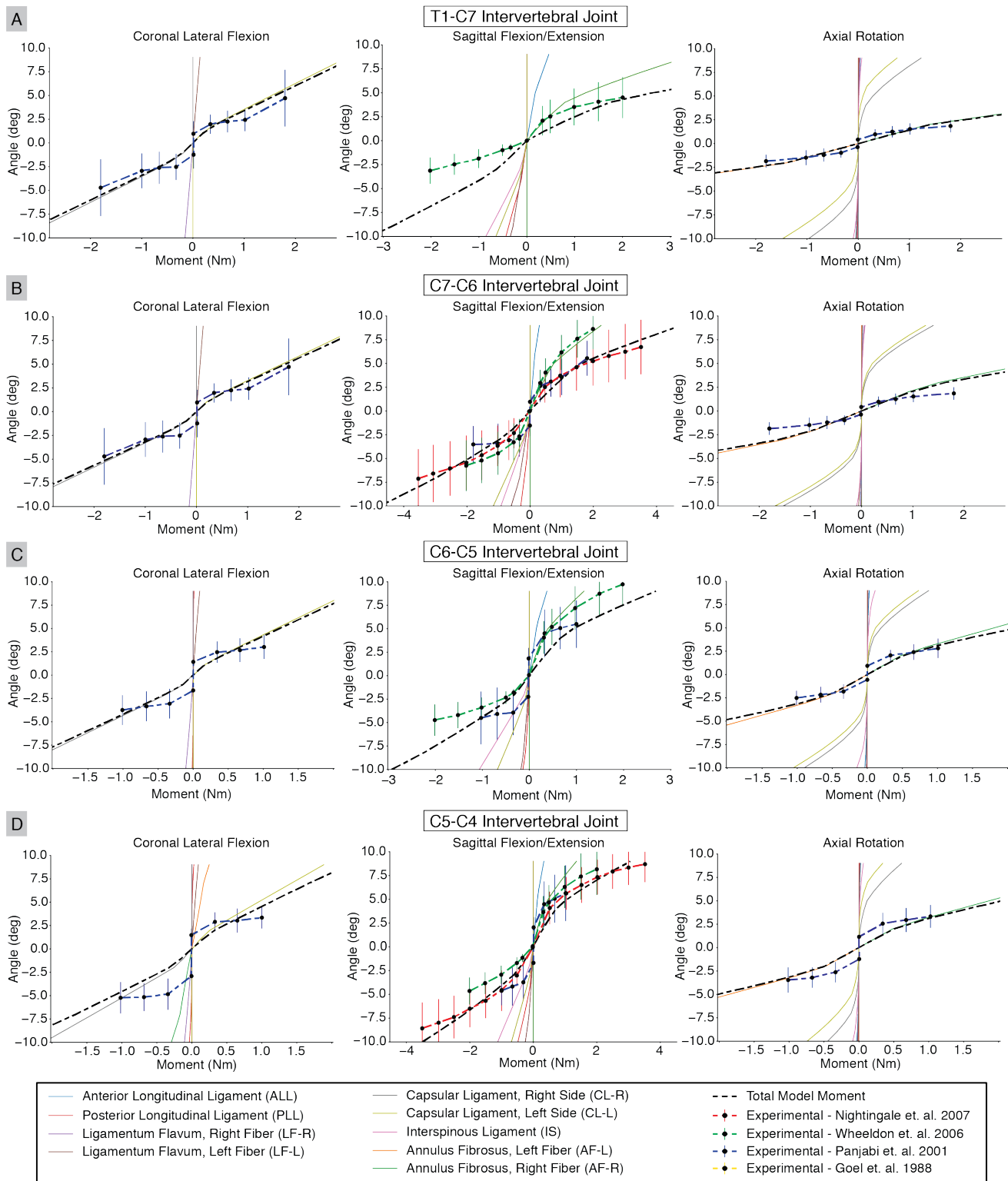


Figure S3: Intersegmental Validation T1-C4: We simulated intervertebral moment-deflection curves to validate our model against experimental data (31, 54–56). The intervertebral functional units contain adjacent vertebrae as well as the ligaments and intervertebral disc. The model ligamentum nuchae is removed to match experimental conditions in (52).

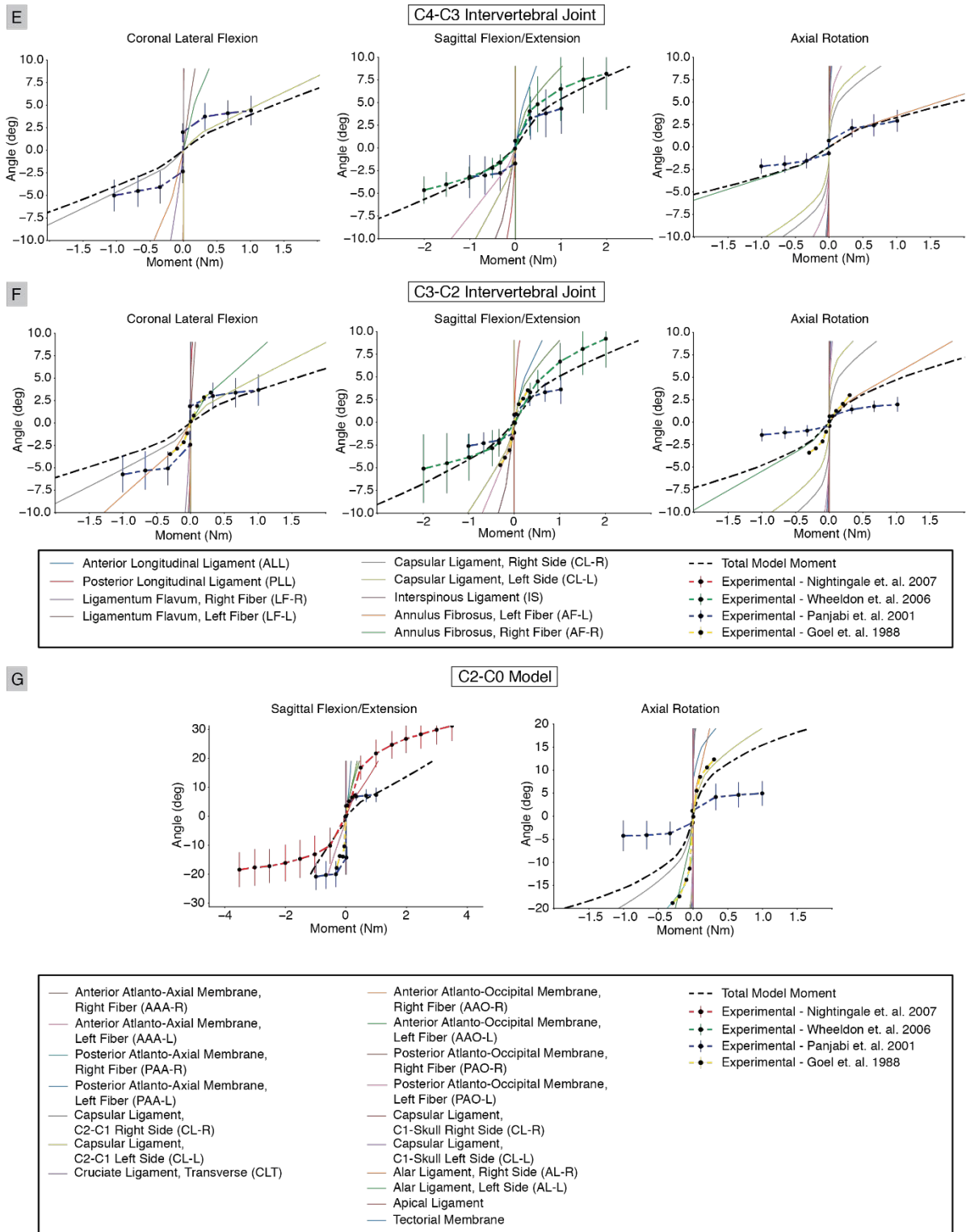


Figure S4: Intersegmental Validation C4-Skull: We simulated intervertebral moment-deflection curves to validate our model against experimental data (31, 54–56). The intervertebral functional units contain adjacent vertebrae as well as the ligaments and intervertebral disc. The model ligamentum nuchae is removed to match experimental conditions in (52). We modeled the full upper cervical spine from C2 through the skull as a single functional unit.

Supplementary Information D: Full Model Evaluation against Experimental Mild Loads

Simulation Analysis. To evaluate the OpenSim simulation of the experimental mild impact loads, we first show an example of the head center of mass trajectory with respect to the torso in each of four conditions (sagittal plane extension with relaxed neck muscles, sagittal plane extension with cocontracted neck muscles, coronal plane lateral flexion with relaxed neck muscles, and coronal plane lateral flexion with cocontracted neck muscles) in one subject (Figure S5). In the experiments, head center of mass trajectory was determined through high speed video tracking, as described in previous work. In the simulation, head center of mass trajectory was extracted directly using forward kinematics. In both cases, the zero position and zero angle were defined as the position and orientation at time zero.

Angular velocity, angular acceleration, and linear acceleration kinematics are more commonly assessed in head impact analysis and thus, we also evaluated OpenSim simulation errors in these kinematic measures. Planar angular velocities and angular acceleration were about the left-right axis in sagittal extension, and about the anterior-posterior axis in coronal lateral flexion. Planar linear accelerations were evaluated at the head center of mass along the anterior-posterior axis in sagittal extension and along the left-right axis in coronal lateral flexion. We did not compare planar linear accelerations along the superior-inferior axis because they were relatively small.

In our experiments, subjects were equipped with an instrumented bite-bar measuring head inertial tri-axial angular velocity and tri-axial linear acceleration at 10kHz with 100ms pre-trigger and 500ms post-trigger. Sensor axes were aligned with anatomical axes (anterior-posterior, left-right, and superior-inferior), and data were filtered with a 50Hz lowpass 4th order butterworth filter. We differentiated angular velocities using a 5-point stencil to obtain angular accelerations. As with the external forces, we average the kinematics time histories over the six trials for each subject and each set of conditions.

Simulated kinematics were extracted directly from the simulations. Angular velocities and angular accelerations were of the skull with respect to the laboratory frame (or the torso frame as the torso was fixed to the laboratory frame). Linear accelerations were of the skull center of mass with respect to the laboratory frame.

We computed four metrics to compare the experimental and simulated kinematics. Before computing these metrics, we first resampled experimental kinematics to 1000Hz with 50ms pre-trigger and 250ms post-trigger ($n = 300$ samples). First, we computed the Pearson's correlation coefficient between the kinematics signals using the Matlab "corr" function. Second, we computed the normalized root mean square (NRMS) error between the experimental (x_{exp}) and simulated (x_{sim}) kinematics, normalizing by the experimental range (equation S1). Third, we computed the normalized error in kinematic range (equation S2). Finally, we compute a CORA (CORrelation Analysis) score, which evaluates similarity based on shape, phase, peaks, and a corridor analysis between the experimental and simulated kinematics (57). Our parameters for computing the CORA scores are provided in Table S4.

$$NRMS = \frac{\sqrt{\frac{\sum n(x_{exp} - x_{sim})^2}{n}}}{\max(x_{exp}) - \min(x_{exp})} \quad \text{eq. S1}$$

$$Range\ Error = \frac{[\max(x_{exp}) - \min(x_{exp})] - [\max(x_{sim}) - \min(x_{sim})]}{\max(x_{exp}) - \min(x_{exp})} \quad \text{eq. S2}$$

Analysis Results. Example traces for average experimental and simulated angular velocities, angular accelerations, and linear accelerations are shown in Figure S6. Analysis shows that simulated kinematics had correlations exceeding 80%, NRMS errors below 40%, peak to peak errors below 50%, and CORA scores exceeding 0.60 (Figure S7).

Table S4: Parameters for Computing CORA scores.

Parameter	Value	Description
T_MIN	50ms	Time window start for CORA, user defined. The start window time was defined as the onset of external loading.
T_MAX	300ms	Time window end for CORA, user defined. The end window time was defined as the end of the simulation, roughly 100ms - 150ms after the external load was finished.
K	2	Corridor score transition method. This is set as a quadratic transition between the inner (score = 1.0) and outer (score = 0.0) corridors.
a_0	0.2	Width of inner corridor. This is the half-width of the inner corridor as a ratio of the peak of the absolute value reference signal.
b_0	0.5	Width of outer corridor. This is the half-width of the outer corridor as a ratio of the peak of the absolute value reference signal.
D_MIN	0.01	Maximum phase shift that is given a score of 1.0 in the phase analysis as a ratio of the total time interval of the signal (250ms in our case yields a 2.5ms allowable phase shift that still yields a phase shift score of 1.0).
D_MAX	0.20	Maximum allowable phase shift. This is given as a ratio of the total time interval of the signal and phase shifts beyond this value are scored as 0.0. (250ms in our case yields a 50ms allowable phase shift).
INT_MIN	0.80	Minimum overlap of the interval. Reference and simulated signals must overlap by the amount given, which is a ratio of the total time interval of the signal (250ms in our case yields a minimum overlap of 200ms).
K_V K_G K_P	1	Correlation, size, and phase shift transition method respectively. This is set as a linear transition between the minimum and maximum scores (0.0 and 1.0 respectively).
G_V G_G G_P	0.2	Weights assigned to the individual correlation, size, and phase shift scores respectively when computing the aggregate score. In our case, we are setting equal weights to each analysis method.
G_1	0.4	Weight assigned to the corridor method score. We set this to 0.4 per the CORA manual recommendation on page 36, section 8.4
G_2	0.6	Weight assigned to the combined correlation, size, and phase method scores. We set this to 0.6 per the CORA manual recommendation on page 36, section 8.4

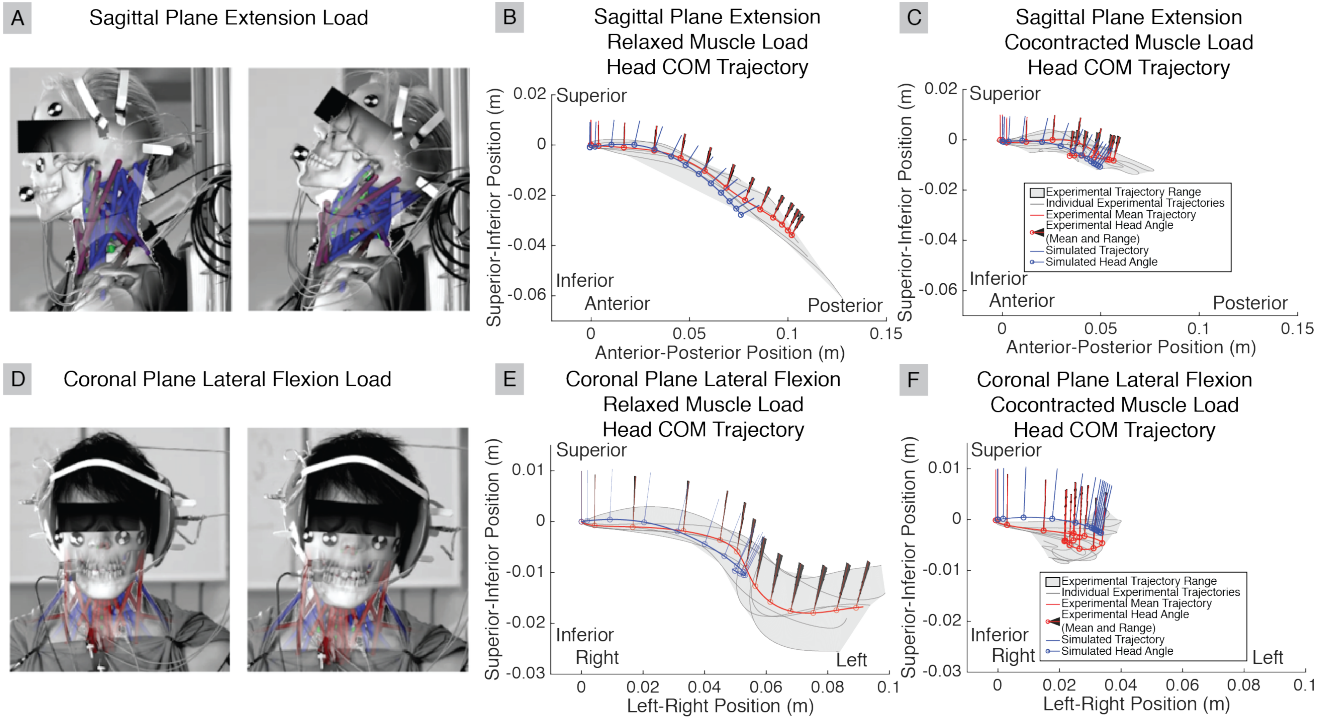


Figure S5: Example Head Center of Mass Trajectories: OpenSim screenshots were overlaid on experimental videos for (A) sagittal extension impacts and (D) coronal plane impacts to qualitatively demonstrate similar behavior. In the experimental videos, we tracked the trajectory of the head center of mass with respect to the torso and the head's orientation with respect to the torso. We compared simulated trajectories against experimental trajectories, with examples of (B) sagittal plane extension load with relaxed muscle activity, (C) sagittal plane extension load with cocontracted muscle activity, (E) coronal plane lateral flexion load with relaxed muscle activity, and (F) coronal plane lateral flexion load with cocontracted muscle activity shown here. In these sample traces, the simulated trajectory falls within the range of trajectories for the six experimental trials within a given condition for a single subject.

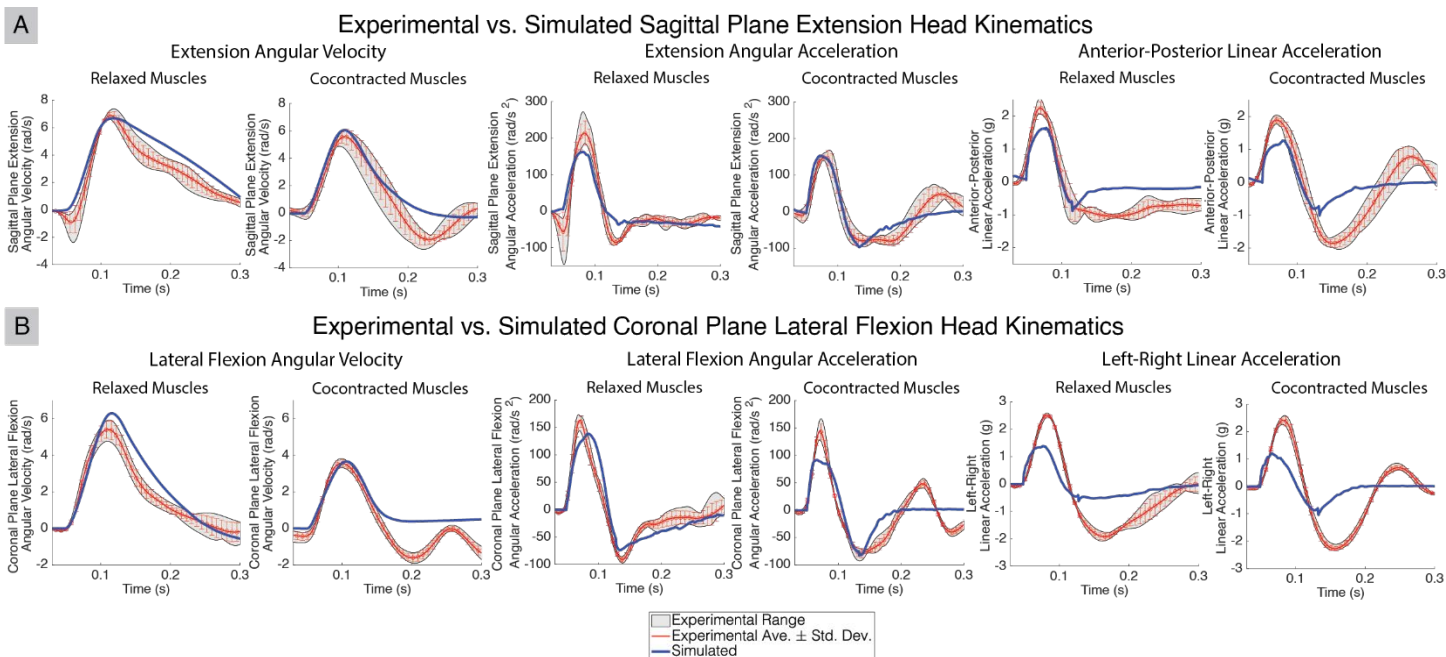


Figure S6: Comparing Sample Experimental and Simulated Kinematics: Sample experimental and simulated kinematics from (A) sagittal extension and (B) coronal lateral flexion also show similar behavior. Planar angular velocity, angular acceleration, and linear accelerations, are all shown for both relaxed muscle and cocontracted muscle conditions. Experimental data were aggregated over the six trials for each condition, with the minimum to maximum range, average, and standard deviation shown here.

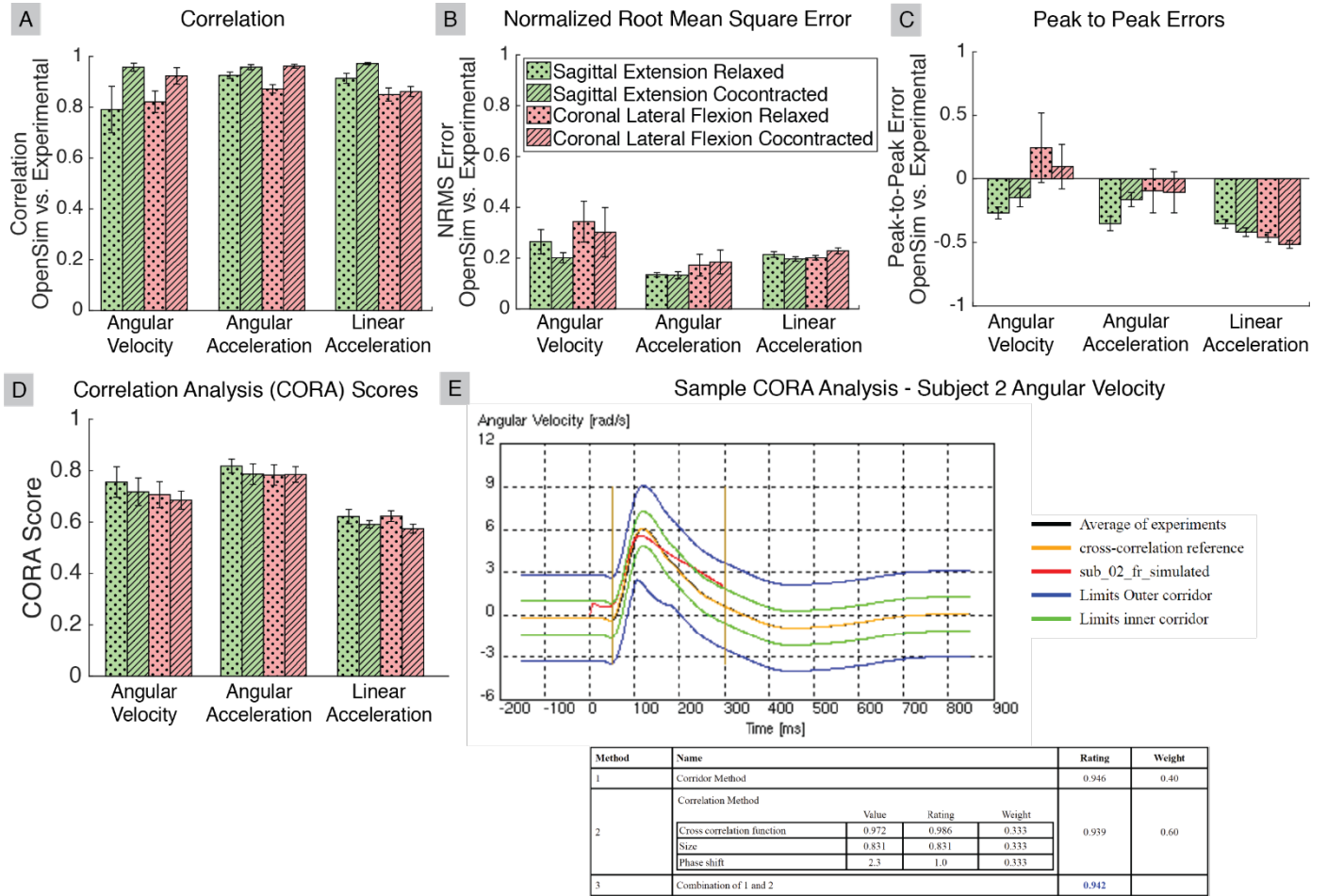


Figure S7: Validation between Simulated OpenSim and Experimental Kinematics: The planar angular velocity, angular acceleration, and linear acceleration at the head center of mass were computed from OpenSim simulations and taken from instrumented bite-bar data in experimental trials. (A) Correlation, (B) NRMS error, (C) peak to peak errors, and (D) CORA scores between OpenSim and experimental kinematics were computed for each condition and aggregated over all 10 subjects (error bars represent standard errors). In most conditions, OpenSim and experimental kinematics had above 80% correlation, below 40% NRMS errors, below 50% peak to peak errors, and CORA scores exceeding 0.6. An example of a CORA analysis for a single subject in angular velocity is presented as an example of how the CORA score weights cross-correlation, size, phase, and corridor scores into a final score.

References:

40. Yoganandan N, Pintar FA, Zhang J, Baisden JL (2009) Physical properties of the human head: mass, center of gravity and moment of inertia. *J Biomech* 42(9):1177–92.
41. Nightingale RW, Camacho DL, Armstrong AJ, Robinette JJ, Myers BS (2000) Inertial properties and loading rates affect buckling modes and injury mechanisms in the cervical spine. *J Biomech* 33(2):191–197.
42. Nightingale RW, McElhaney JH, Richardson WJ, Myers BS (1996) Dynamic responses of the head and cervical spine to axial impact loading. *J Biomech* 29(3):307–318.
43. Saari A, et al. (2013) Compressive Follower Load Influences Cervical Spine Kinematics and Kinetics During Simulated Head-First Impact in an in Vitro Model. *J Biomech Eng* 135(11):111003.
44. Mattucci SFE, Moulton JA, Chandrashekar N, Cronin DS (2013) Strain rate dependent properties of human craniovertebral ligaments. *J Mech Behav Biomed Mater* 23:71–79.
45. Panjabi MM, White AA, Johnson RM (1975) Cervical spine mechanics as a function of transection of components. *J Biomech* 8(5):327–336.
46. Mercer S, Bogduk N (1999) The ligaments and annulus fibrosus of human adult cervical intervertebral discs. *Spine (Phila Pa 1976)* 24(7):619-26; discussion 627–8.
47. Pooni J, Hukins D, Harris P, Hilton R, Davies K (1986) Comparison of the structure of human intervertebral discs in the cervical, thoracic and lumbar regions of the spine. *Surg Radiol Anat* 8(3):175–182.
48. Mattucci SFE, Moulton JA, Chandrashekar N, Cronin DS (2012) Strain rate dependent properties of younger human cervical spine ligaments. *J Mech Behav Biomed Mater* 10:216–226.
49. DVORAK J, PANJABI MM (1987) Functional Anatomy of the Alar Ligaments. *Spine (Phila Pa 1976)* 12(2):183–189.
50. Zhang QH, Teo EC, Ng HW, Lee VS (2006) Finite element analysis of moment-rotation relationships for human cervical spine. *J Biomech* 39(1):189–193.
51. del Palomar AP, Calvo B, Doblare M (2008) An accurate finite element model of the cervical spine under quasi-static loading. *J Biomech* 41(3):523–531.
52. Bass CR, et al. (2007) Failure properties of cervical spinal ligaments under fast strain rate deformations. *Spine (Phila Pa 1976)* 32(1):7–13.
53. Chazal J, et al. (1985) Biomechanical properties of spinal ligaments and a histological study of the supraspinal ligament in traction. *J Biomech* 18(3):167–176.
54. Goel VK, Clark CR, Gallaes K, Liu YK (1988) Moment-rotation relationships of the ligamentous occipito-atlanto-axial complex. *J Biomech* 21(8). doi:10.1016/0021-9290(88)90204-7.
55. Nightingale RW, et al. (2007) Flexion and extension structural properties and strengths for male cervical spine segments. *J Biomech* 40(3):535–42.
56. Wheeldon JA, Pintar FA, Knowles S, Yoganandan N (2006) Experimental flexion/extension data corridors for validation of finite element models of the young, normal cervical spine. *J Biomech* 39(2):375–380.
57. Gehre C, Gades H, Wenicke P (2009) Objective Rating of Signals Using Test and Simulation Responses. *Enhanced Safety of Vehicles Conference*, pp 1–8.